ELSEVIER

Synthetic Metals 116 (2001) 343–347

SYNTHETIC METALS

www.elsevier.com/locate/synmet

Photovoltaic cells based on ionically self-assembled nanostructures

T. Piok[a,b,*], C. Brands[a], P.J. Neyman[a], A. Erlacher[a,b], C. Soman[a], M.A. Murray[a], R. Schroeder[a], W. Graupner[a], J.R. Heflin[a], D. Marciu[c], A. Drake[c], M.B. Miller[c], H. Wang[d], H. Gibson[d], H.C. Dorn[d], G. Leising[b], M. Guzy[e], R.M. Davis[e]

[a]*Department of Physics, Virginia Tech., Blacksburg, VA 24061-0435, USA*
[b]*Institut für Festkörperphysik, Technische Universität Graz, Graz 8010, Austria*
[c]*Luna Innovations, Inc., P.O. Box 11704, Blacksburg, VA 24062-1704, USA*
[d]*Department of Chemistry, Virginia Tech, Blacksburg, VA 24061-0212,USA*
[e]*Department of Chemical Engineering, Virginia Tech., Blacksburg, VA 24061-0211, USA*

Abstract

We use the technique of ionically self-assembled monolayers (ISAMs) to produce photovoltaic devices of well-controlled thickness and composition. The ISAM nanostructure fabrication method simply involves the alternate dipping of a charged substrate into aqueous cationic and anionic solutions at room temperature. We have employed several approaches to combine the tetrahydrothiophenium precursor of poly(*para*-phenylene-vinylene) (PPV) with fullerenes and other organic materials. We apply modulation spectroscopy for the electro-optical characterization of the ISAM-devices. The modulation frequency dependence of the photocurrent can be assigned to the influence of trapped charges taking part in the photovoltaic process. © 2001 Published by Elsevier Science B.V.

Keywords: Photovoltaics; Polyelectrolytes; Ionically self-assembled monolayers; Poly(*para*-phenylene-vinylene); Fullerenes

1. Introduction

The ultrafast photoinduced electron transfer between conjugated molecules of appropriately chosen levels of the highest occupied molecular orbital (HOMO) and the lowest unoccupied molecular orbital (LUMO) has allowed the production of efficient organic photovoltaic devices [1,2]. Although there has been rapid progress in recent years, very fundamental questions of optical charge generation and transport in organic materials are not yet resolved, which span fields from quantum mechanics to chemical engineering [3–6]. The absorption of light in a conjugated polymer primarily creates bound electron–hole pairs in their singlet state, singlet excitons (SE). It has become clear that the charge generation process in ''pure'' layers of conjugated molecules is driven by defects which serve as exciton dissociation centers [7,8]. In this sense, the incorporation of an electron accepting guest, such as the pure fullerene C_{60} [9], derivatized fullerenes [10–12] or others [13] in a poly(-*para*-phenylene-vinylene) (PPV) host can be seen as an introduction of ''defects''. Since the exciton diffusion length in conjugated polymers is on the order of 10 nm [14], however, the charge generation can only occur if the dissociation site is within this distance of any given optically excited electron–hole pair.

A special variation of the dip coating approach produces exceptionally homogeneous thin films through the ionically self-assembled monolayer (ISAM) process. This method was developed by Decher and coworkers [15,16] and used for polymer light emitting diodes by Rubner and coworkers [17,18] as well as for nonlinear optical applications by us [19–21]. The ISAM method involves the alternate dipping of a charged substrate into an aqueous solution of a cation followed by dipping in an aqueous solution of an anion at room temperature (see Fig. 1).

2. Experimental

In a related detailed study, the parameters of the dipping solutions for the absorbance of the films and thus, the thickness of the films were optimized [22]. In general, the ISAM layer structure is described by the scheme in Fig. 1. In particular, we show a bilayer system based on PPV and $C_{60}(OH)_{24}$. The data for the samples used in this study are compiled in Table 1. All optical and electrical measurements were performed in air at room temperature.

* Corresponding author.

0379-6779/01/$ – see front matter © 2001 Published by Elsevier Science B.V.
PII: S0379-6779(00)00434-3

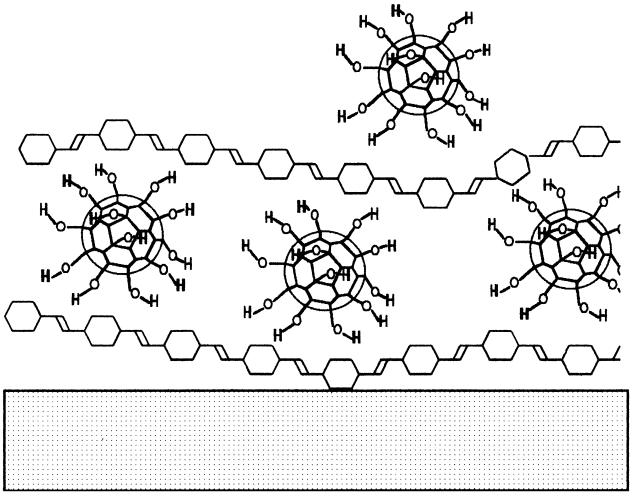

Fig. 1. Composition of the PPV-$C_{60}(OH)_{24}$ ISAM films on a molecular level. This is a "magnification" of the schematic bilayer structure. The grey area represents the substrate.

The basic constituents of the ISAM films in this study are PPV and poly(methacrylic acid) (PMA) as oppositely charged film forming agents. The conjugated PPV precursor is prepared via the classic route [23] and has already been used successfully for ISAM-based devices [17]. PMA was purchased from Polysciences. For an interface study, which was also conducted for light emitting diodes [22], we used several polymers. The polythiophene acetic acid (PTAA) was prepared according to [24]. Poly(allylamine hydrochloride) (PAH) and Cu-phthalocyanine tetrasulfonic acid tetrasodium salt were purchased from Aldrich, and poly(sodium 4-styrenesulfonate) (PSS) was purchased from Polysciences. We have chosen $C_{60}(OH)_n$ as a water-soluble ionizable fullerene derivative which was purchased from MER Corporation in Tucson, AZ. When $C_{60}(OH)_n$ is synthesized, it yields a range of products which are not easily separated. The product we have used has an n-range of 22–26 for average composition of $C_{60}(OH)_{24}$. The pH and the ionic strength were adjusted as described below for the different studies. We will only report a selection of these parameters, which are described comprehensively in [22]. The film preparation process is described in detail in [25].

Table 1
Overview of a selection of the samples used in this investigation[a]

Sample no.	Sample composition	Peak response (10^{-5} A/W)
1	$(PPV/PMA)_{10}$	1
2	$(PPV/PMA)_{20}$	4
3	$(PPV/PMA)_{40}$	3.6
4	$(PPV/PMA)_{32}$	90[b]
5	$(PPV/C_{60}(OH)_{24})_{32}$	0.55
6	$(PPV/C_{60}(OH)_{24})_{32}$	32[b]
7	$(PAH/PT)_3(PPV/PMA)_{20}$	34[b]
8	$(PAH/PSS)_3(PPV/PMA)_{20}$	55[b]
9	$(PPV/PMA)_{20}$	19[b]
10	$(PPV/PMA)_{20}(PAH/PT)_{20}$	12[b]
11	$(PPV/PMA)_{20}(PAH/PSS)_3$	36[b]
12	$(PPV/CuPc)_{30}$	170[b]
13	$(PPV/CuPc/PPV/PMA)_{15}$	30[b]
14	$(PPV/PMA)_{30}$	20[b]

[a] The peak response describes the maximum photocurrent for each of the 14 classes of devices we have investigated. Furthermore, we want to note that the photocurrent action spectra are normalized to the incident intensity and not to the absorbed intensity. We have used the following terminology: $(A/B)_x$, where A, B denote the constituents of the bilayers and x denotes the number of bilayers.

[b] Characterizes "thick" films [25].

The photovoltaic characterization was done with an Oriel 66,002 light source, using a 150 W ozone free Xe lamp. The beam was passed through quartz lenses, an optical chopper and a CM 110 monochromator, equipped with a 2400 grooves per line grating, blazed at 250 nm. The area of the illuminated spot on the sample was 3 mm^2 with the excitation density on the order of 330 $\mu W/cm^2$. For the modulation measurements, we used a chopper-frequency of 42 Hz. The photocurrent signal was picked up by a Stanford Research System lock-in amplifier SR 830.

For the optical characterization, we have used an F20-UV thin-film measurement system by Filmetrics. The measurements yield two spectra:

1. The reflection spectrum $R(\lambda)$ — i.e. the fraction of light reflected by the complete layered structure.
2. The transmission spectrum $T(\lambda)$ — i.e. the fraction of light transmitted through the complete layered structure. These two spectra can be used *to calculate*:
3. The absorption spectrum $A(\lambda)$ — i.e. the fraction of light absorbed by the complete layered structure.

The calculation of $A(\lambda)$ is based on the assumption that $1 = A(\lambda) + T(\lambda) + R(\lambda)$.

3. Results and discussion

Fig. 2 shows the photocurrent action spectra as well as the optical spectra of the thin device layers (sample nos. 1–3 in Table 1) in the region where no Al is deposited. The photocurrent response for these devices as well as the others is summarized in Table 1. The very low absolute values of the photocurrent response for all three samples can be understood easily when looking at the optical data. The very thin ISAM films do not show any signature of absorption by the PPV: we show this by plotting $1 - A(\lambda)$, which represents the transmitted intensity after correction for reflection. The reflectivity clearly shows the presence of the very thin PPV film — the dips in the transmission spectra are primarily due to the peaks in the reflection, which are caused by the strong dispersion in the resonant region. Also, the photocurrent action spectra clearly show the onset for the PPV photocurrent at around 525 nm. The apparent peak in photovoltaic response at 330 nm is characteristic for the device and not for the PPV, since we normalize our spectra with the incident radiation and not with the absorbed one.

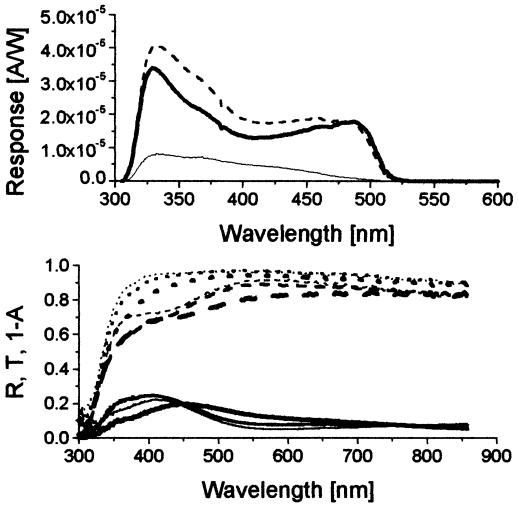

Fig. 2. Top: photocurrent action spectra of the thin $(PPV/PMA)_n$ devices: thin line, $n = 10$; dashed line, $n = 20$; thick solid line, $n = 40$. Bottom: measured reflection spectrum $R(\lambda)$ — solid lines; measured transmission spectrum $T(\lambda)$ — dashed lines; calculated $R(\lambda) + T(\lambda)$ — dotted lines. The latter corresponds to $1 - A(\lambda)$. The different line thickness denotes the three devices: thin line, $n = 10$; medium line, $n = 20$; thick line: $n = 40$.

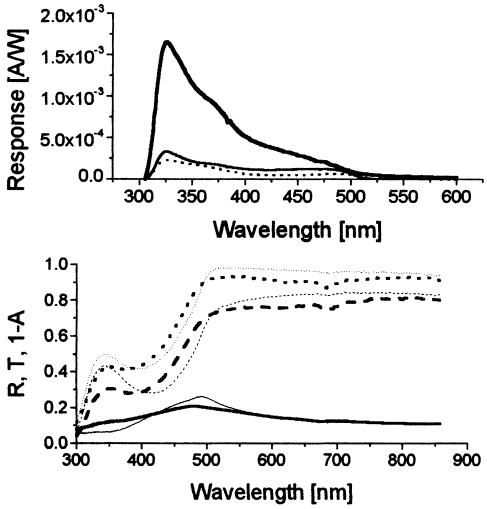

Fig. 4. Top: photocurrent action spectra of $(PPV/CuPc)_{30}$ (thick line) and $(PPV/CuPc/PPV/PMA)_{15}$ (thin line). The dotted line shows the response of a $(PPV/PMA)_{30}$ for comparison. Bottom: measured $R(\lambda)$ (solid lines); $T(\lambda)$ (dashed lines); calculated $R(\lambda) + T(\lambda) = 1 - A(\lambda)$ (dotted lines). The thick and thin lines refer to $(PPV/CuPc)_{30}$ and $(PPV/CuPc/PPV/PMA)_{15}$, respectively.

Therefore, the strong decrease in photovoltaic response in these and all the following spectra represents the absorbance by glass and ITO. In order to obtain thicker films, we changed the film formation parameters as described in [25].

The suppression of the observed electrical and optical PPV signatures is also observed in a thick sample, consisting of 32 bilayers of $(PPV/C_{60}(OH)_{24})$ as shown in Fig. 3. In addition, also the time-constants observed in these devices are completely different from what is observed for the thick $(PPV/PMA)_{32}$ devices. Therefore, the $(PPV/C_{60}(OH)_{24})_n$ devices contain relatively low amounts of PPV — we are observing the photovoltaic properties of $C_{60}(OH)_{24}$. In order to overcome this shortcoming, $(PPV/PMA/PPV/C_{60}(OH)_{24})_n$ devices are being produced. However, there are also other potential molecular dopands, which are expected to increase the photovoltaic response. We have decided to use Cu-phthalocyanine tetrasulfonic acid tetrasodium salt (CuPc) and report the results in Fig. 4.

The inclusion of CuPc into the production process of thick PPV films at two levels of concentration results in a clear improvement of the photocurrent response as we use a higher CuPc concentration and does not inhibit the PPV deposition as observed for the inclusion of $C_{60}(OH)_{24}$. The optical spectra in Fig. 4 confirm all the assumptions made about the film production process. The absorption peak at 690 nm stems from CuPc and confirms its presence in the film. The strength also scales with the CuPc concentration, supporting the expected 2:1 ratio for the CuPc concentration in the $(PPV/CuPc)_{30}$ and $(PPV/CuPc/PPV/PMA)_{15}$ devices.

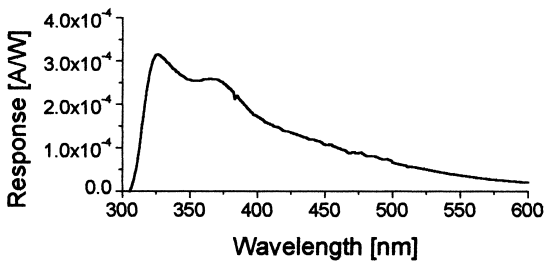

Fig. 3. Photocurrent action spectra of the thick $(PPV/C_{60}(OH)_{24})_{32}$ devices.

We have used a phase-sensitive modulation technique (lock-in amplifier) for the optoelectronic characterization of the devices. In general, every experiment of this kind yields two results — a signal intensity and a phase shift. The influence of a time-constant or lifetime τ on the signal vector R measured in a typical modulation experiment with a lock in amplifier can be described in the following manner if two time-constants are involved

$$R = \frac{c_1\{\exp[i\tan^{-1}(2\pi f\tau_1)]\}}{\sqrt{1+(2\pi f\tau_1)^2}} + \frac{c_2\{\exp[i\tan^{-1}(2\pi f\tau_2)]\}}{\sqrt{1+(2\pi f\tau_2)^2}} \quad (1)$$

where R is the intensity of the signal, f the modulation frequency, τ_1 and τ_2 are the lifetimes of the involved species or time-constants, as introduced to diodes via their depletion layer capacitance. Furthermore, c_1 and c_2 represent the weight of each component. If there are two time-constants involved, it means that there is an initial branching in the population into two separate *uncoupled* states, which decay with different decay rates. The physical meaning is that there is no single state with one lifetime but there are uncoupled states with different lifetimes. With respect to optoelectronic device characterization, one has to emphasize that a lifetime of the charge carriers (τ_1) and a device time-constant, caused

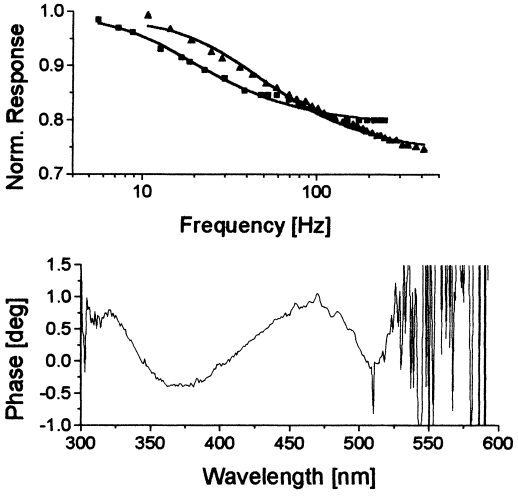

Fig. 5. Top: normalized photocurrent vs. chopper frequency for the thick $(PPV/PMA)_{32}$ devices. Triangles denote the results obtained for the excitation wavelength $\lambda_{exc} = 500$ nm, squares refer to $\lambda_{exc} = 350$ nm. Bottom: Phase angle of the spectrally resolved photocurrent.

by the capacitance and resistance ($RC = \tau_2$), would exactly add up in the described way of $1/\tau_{total} = 1/\tau_1 + 1/\tau_2$.

If the second decay-time τ_2 is very small compared to the largest value used for the inverse modulation frequency, we can set τ_2 equal to zero (see modeling in Figs. 5 and 6 and Table 2). The τ_2-related process does not influence the phase θ of the signal

$$I = \frac{c_1}{\sqrt{1 + (2\pi f \tau_1)^2}} + c_2 \quad (2)$$

$$\theta = \tan^{-1}(2\pi f \tau) \quad (3)$$

Before we show how these equations perfectly describe the experimental behavior, we want to emphasize the physical

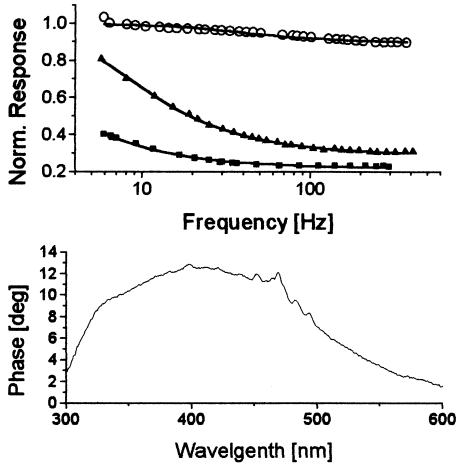

Fig. 6. Top: normalized photocurrent vs. chopper frequency for the thick $(PPV/C_{60}(OH)_{24})_{32}$ devices. Open circles denote the results obtained for the excitation wavelength $\lambda_{exc} = 580$ nm; triangles refer to $\lambda_{exc} = 500$ nm; squares refer to $\lambda_{exc} = 350$ nm. Bottom: Phase angle of the spectrally resolved photocurrent.

Table 2
A selection of parameters extracted from the analyses of the frequency dependent data in Figs. 5 and 6[a]

Device	λ_{exc} (nm)	c_1	τ_1 (ms)	c_2
$(PPV/PMA)_{32}$-thick	350	0.20	12	0.80
$(PPV/PMA)_{32}$-thick	500	0.25	4.9	0.75
$(PPV/C_{60}(OH)_{24})_{32}$-thick	350	0.78	110	0.22
$(PPV/C_{60}(OH)_{24})_{32}$-thick	500	0.71	27	0.29
$(PPV/C_{60}(OH)_{24})_{32}$-thick	580	0.10	6	0.90

[a] The modeling is based on Eq. (2). The weights c_1 and c_2 have been normalized, so that $c_1 + c_2 = 1$, $\tau_2 = 0$ ms.

interpretation of this formalism:

1. The number of decay-times and their values found in the photocurrent modulation experiments express the number of different states and their contribution to the process of charge transport in the photovoltaic devices.
2. Modeling the recorded $I(f)$ curves allows us to retrieve a very important additional piece of information: the quasi-steady value of the photocurrent which can be obtained by extrapolating to $f = 0$.

In Fig. 5, we show the dependence of the photocurrent on the chopper frequency at λ_{exc} of 350 and 500 nm for the thick $(PPV/PMA)_{32}$ devices. These curves can be modeled with Eq. (2) — the results are shown in Table 2. At $\lambda_{exc} = 500$ nm the frequency-independent part — associated with the time-constant $\tau_2 = 0$ s — is slightly weaker than at 350 nm (weight of 0.75 versus 0.80). The time-constant of the frequency dependent part is 4.9 ms at 500 nm as compared to 12 ms at 350 nm.

The thin PPV devices did not show any frequency dependence of the photocurrent for chopper frequencies between 4 and 400 Hz, in accordance to its very small phase angle. We will, therefore, present the results for devices which showed a large phase angle of the photocurrent: the thick $(PPV/C_{60}(OH)_{24})_{32}$ devices — see Fig. 6. The weakest frequency dependence is observed at 580 nm (smallest phase angle of $\approx 2^\circ$) and the strongest frequency dependence is observed at 350 nm (largest phase angle of $\approx 10^\circ$).

In summary, we have described how to produce thin and thick ISAM films with a comparable amount of bilayers and quantitatively discussed the influence of thickness and incorporating other materials into the ISAM layers. Moreover, we have given a detailed description of the optical properties of the devices. Finally, we have shown how the time constants influence the photovoltaic process.

Acknowledgements

Support by Air Force SBIR F49620-98-C-0074, NSF Science and Technology Center DMR 9120004, VA Tech 1999 Aspires, Austrian Ministry for Science (A.E. and T.P.). W.G. acknowledges exciting interaction with R. Gonzalez.

References

[1] C.W. Tang, Appl. Phys. Lett. 48 (1986) 83.
[2] M. Granstrom, K. Petritsch, A.C. Arias, A. Lux, M.R. Andersson, R.H. Friend, Nature 395 (1998) 257.
[3] A. Köhler, D.A. dos Santos, D. Beljonne, Z. Shuai, J.-L. Bredas, A.B. Holmes, A. Kraus, K. Müllen, R.H. Friend, Nature 392 (1998) 903–906.
[4] D. Moses, J. Wang, G. Yu, A.J. Heeger, Phys. Rev. Lett. 80 (1998) 2685.
[5] W. Graupner, G. Cerullo, M. Nisoli, G. Lanzani, E.J.W. List, G. Leising, S. De Silvestri, Phys. Rev. Lett. 81 (1998) 3259–3262.
[6] V.I. Arkhipov, E.V. Emelianova, H. Bässler, Phys. Rev. Lett. 82 (1999) 1321.
[7] E. Frankevich, A. Zakhidov, K. Yoshino, Y. Maruyama, K. Yakushi, Phys. Rev. B 53 (1996) 4498.
[8] B. Dulieu, J. Wéry, S. Lefrant, J. Bullot, Phys. Rev. B 57 (1998) 9118.
[9] N.S. Sariciftci, D. Braun, C. Zhang, V.I. Srdanov, A.J. Heeger, G. Stucky, F. Wudl, Appl. Phys. Lett. 62 (1993) 585–587.
[10] G. Yu, A.J. Heeger, J. Appl. Phys. 78 (1995) 4510–4515.
[11] G. Yu, J. Gao, J.C. Hummelen, F. Wudl, A.J. Heeger, Science 270 (1995) 1789–1791.
[12] J.J.M. Halls, C.A. Walsh, N.C. Greenham, E.A. Marseglia, R.H. Friend, S.C. Moratti, A.B. Holmes, Nature 376 (1995) 498–500.
[13] A.C. Arango, S.A. Carter, P.J. Brock, Appl. Phys. Lett. 74 (1999) 1698.
[14] A. Haugeneder, M. Neges, C. Kallinger, W. Spirkl, U. Lemmer, J. Feldmann, U. Scherf, E. Harth, A. Gügel, K. Müllen, Phys. Rev. B 59 (1999) 15346.
[15] G. Decher, J.D. Hong, Makromol. Chem., Makromol. Chem. Symp. 46 (1991) 321.
[16] G. Decher, J.D. Hong, J. Schmitt, Thin Solid Films 210/211 (1992) 831.
[17] A.C. Fou, O. Onitsuka, M. Ferreira, M.F. Rubner, B.R. Hsieh, J. Appl. Phys 79 (1996) 7501.
[18] J-K. Lee, D. Yoo, M.F. Rubner, Chem. Mater. 9 (1997) 1710.
[19] J.R. Heflin, C. Figura, D. Marciu, Y. Liu, R.O. Claus, Appl. Phys. Lett. 74 (1999) 495.
[20] K.M. Lenahan, Y. Wang, Y. Liu, R.O. Claus, J.R. Heflin, D. Marciu, C. Figura, Adv. Mater. 10 (1998) 853.
[21] J.R. Heflin, Y. Liu, C. Figura, D. Marciu, R.O. Claus, SPIE Proc. 3147 (1997) 10.
[22] D. Marciu, M. Miller, A.L. Ritter, M.A. Murray, P.J. Neyman, W. Graupner, J.R. Heflin, H. Wang, H.W. Gibson, R.M. Davis, SPIE Proc. 3938 (2000) 169–179.
[23] F.R. Denton III, P.M. Lahti, F.E. Karasz, J. Polym. Sci. Part A: Polym. Chem. 30 (1992) 2223.
[24] A.T. Royappa, M.F. Rubner, Langmuir 8 (1992) 3169.
[25] C. Brands, T. Piok, P.J. Neyman, A. Erlacher, C. Soman, M.A. Murray, R. Schroeder, J.R. Heflin, W. Graupner, D. Marciu, A. Drake, M.B. Miller, H. Wang, H. Gibson, H.C. Dorn, G. Leising, M. Guzy, R.M. Davis, SPIE Proc. 3937 (2000) 51–62.